Infrared Semiconductor 3-5 µm High Power InAsSb Based Injection Lasers

M. Razeghi

Northwestern University
Center for Quantum Devices
2225 N. Campus Drive, MLSB Room 4051
Evanston, IL 60208-3129

March 2002

Final Report

AIR FORCE RESEARCH LABORATORY
Directed Energy Directorate
3550 Aberdeen Ave SE
AIR FORCE MATERIEL COMMAND
KIRTLAND AIR FORCE BASE, NM 87117-5776

AFRL-DE-TR-2002-1023

This report has been approved for publication.

RON KASPI, DR-III
Project Manager

JEFFREY SALTER, CAPT, USAF
Chief, Tactical Laser Branch

R. EARL GOOD, SES
Director, Directed Energy

REPORT DOCUMENTATION PAGE

Form Approved
OMB No. 0704-0188

1. REPORT DATE *(DD-MM-YYYY)*	2. REPORT TYPE	3. DATES COVERED *(From - To)*
March 2002	Final Report	March 2000 – March 2002

4. TITLE AND SUBTITLE

Infrared Semiconductor 3-5 µm High Power InAsSb Based Injection Lasers

5a. CONTRACT NUMBER
F29601-00-C-0004

5b. GRANT NUMBER

5c. PROGRAM ELEMENT NUMBER
62601F

6. AUTHOR(S)
M. Razeghi

5d. PROJECT NUMBER
3326

5e. TASK NUMBER
LP

5f. WORK UNIT NUMBER
AA

7. PERFORMING ORGANIZATION NAME(S) AND ADDRESS(ES)

Northwestern University
Center for Quantum Devices
2225 N. Campus Drive, MLSB Room 4051
Evanston, IL 60208-3129

8. PERFORMING ORGANIZATION REPORT NUMBER

9. SPONSORING / MONITORING AGENCY NAME(S) AND ADDRESS(ES)

AFRL/DELS
3550 Aberdeen Ave SE
Kirtland AFB NM 87117-5776

10. SPONSOR/MONITOR'S ACRONYM(S)

11. SPONSOR/MONITOR'S REPORT NUMBER(S)
AFRL-DE-TR-2002-1023

12. DISTRIBUTION / AVAILABILITY STATEMENT

Approved for public release; distribution unlimited

13. SUPPLEMENTARY NOTES

14. ABSTRACT
The objective of this work is to develop high power, high temperature semiconductor injection mid-infrared lasers through the growth and characterization of Sb-based strained layer superlattice (SLS) laser structures at 4 µm operating in continuous wave mode at room temperature. Our approach is to use lasers employing strained layer superlattice active regions made from InAs/InAsSb, InAsSb/InAsSb and InAsP/InAsSb alloys.
Single step MOCVD growth has been used for the growth of the lasers. The quality of the InAsSbP based materials has been appraised by structural, optical and electrical characterization techniques. Lasers structures based on the InAsSbP material system have been grown, fabricated and tested. Lasers fabricated with the InAsP/InAsSb superlattice alloy produced laser oscillation at $\lambda = 4.0$ µm with output powers as high as 546 mW and 94 mW in pulsed and cw modes respectively. The InAs/InAsSb superlattice alloy also has been used for the active region of lasers with $\lambda = 3.8$-4.0.
At low temperature, these lasers emit with very high power: up to 1.0 W with $\lambda = 3.8$ µm and 842 mW with $\lambda = 4.0$ µm.
Finally, InAsSb/InAsSb superlattice lasers have also been employed and have demonstrated a wide range of emission flexibility. Laser oscillation between 4.2 and 4.8 µm have been measured with powers as high as 460 mW.

15. SUBJECT TERMS
Semiconductor Laser, mid-infrared, InAsSb, high power

16. SECURITY CLASSIFICATION OF:			17. LIMITATION OF ABSTRACT	18. NUMBER OF PAGES	19a. NAME OF RESPONSIBLE PERSON
a. REPORT Unclassified	**b. ABSTRACT** Unclassified	**c. THIS PAGE** Unclassified	Unlimited	44	Ron Kaspi

19a. NAME OF RESPONSIBLE PERSON: Ron Kaspi

19b. TELEPHONE NUMBER *(include area code)*
(505) 272-7822

Standard Form 298 (Rev. 8-98)
Prescribed by ANSI Std. 239.18

Table of Contents

Table of Figures

vi

1. Modeling of the strained layer superlattice active regions

Despite the need for coherent emitters in the 4-5 μm wavelength region, additional increases in emission wavelength have been found to be difficult with conventional interband emitter (Double Heterostructure, DH, and Multiple Quantum Well, MQW) structures. For DH lasers emitting at $\lambda > 3.4$ μm, the misfit dislocations between the $InAs_xSb_yP_{1-x-y}$ cladding and $InAs_xSb_{1-x}$ active region are increased to levels that prohibit oscillation. MQW emitters have demonstrated the ability to emit spontaneously covering the entire 3-5 μm region. This is shown below in Figure 1 in which the antimony composition was varied in the quantum wells (InAsSb) of an $InAs/InAs_xSb_{1-x}$ MQW structure. The cladding region was InAsSbP in all five structures.
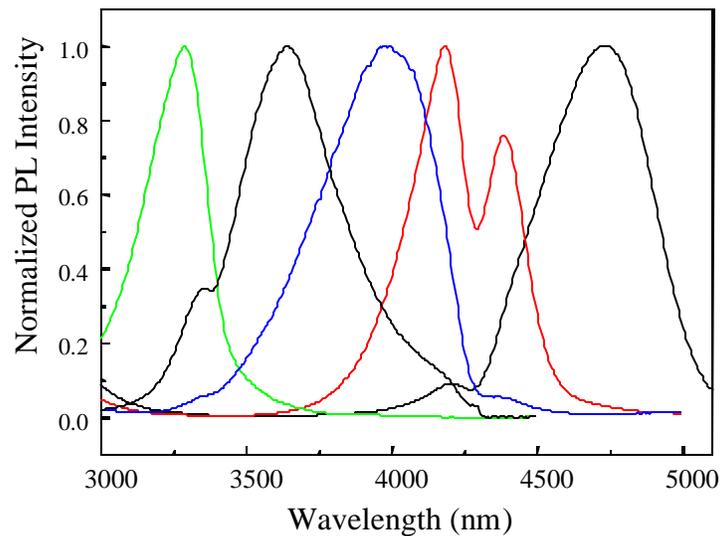
Figure 1. PL spectra for 5 MQW structures demonstrating the ability to cover the entire 3-5 mm wavelength region.

This is a result of the fact that MQW structures can accommodate a larger percent mismatch between active and barrier regions than DH structures as long as the thickness of the quantum well is thinner than the critical thickness. The critical thickness of $InAs/InAs_xSb_{1-x}$ has been calculated using the Matthews-Blakeslee and People-Bean relationships.[i,ii] The experimental results are much better fit to the People-Bean relationship, which is shown in Figure 2.

$$d_c = \frac{(1-v)b^2 \ln(d_c/b)}{8\pi w f^2 (1+v)}$$
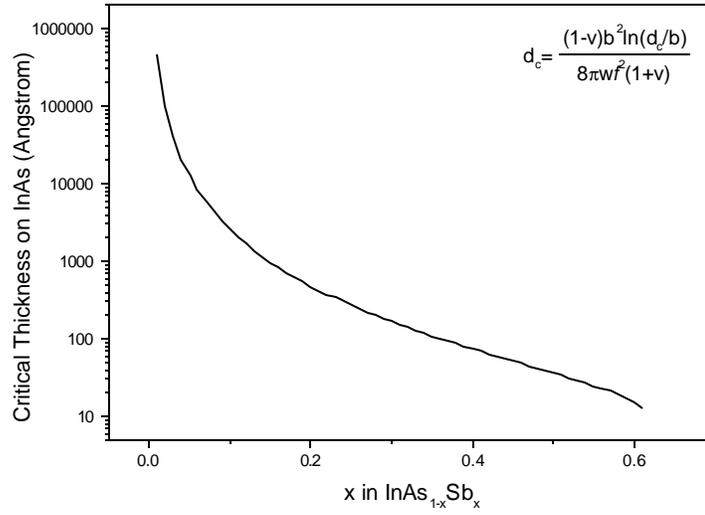
Figure 2. Calculated critical thickness of InAs$_{1-x}$Sb$_x$ on InAs.

Also, the emission wavelength for bulk InAsSb is shown in Figure 3. It shows that around 20 % antimony must be incorporated into a bulk active region for emission up to 5 µm.
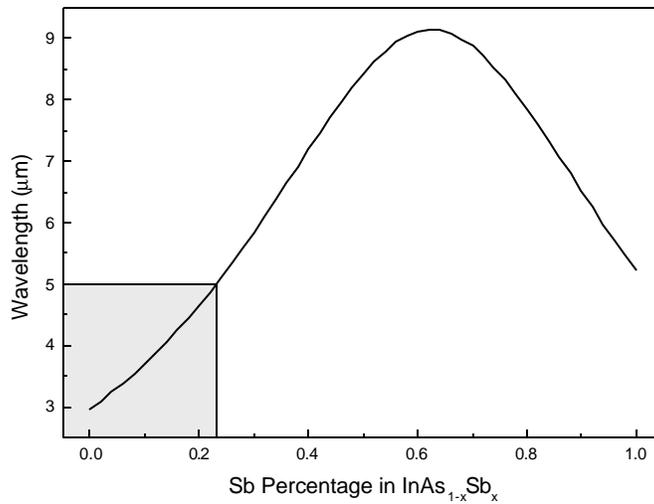
Figure 3. Emission wavelength for bulk InAs$_{1-x}$Sb$_x$ as a function of antimony composition at 78 K. The shaded area shows the required compositions to cover the 3-5 mm region.

From Figure 2 and Figure 3, the critical thickness of InAs$_{0.8}$Sb$_{0.2}$ is approximately 100 Å. However using these dimensions, the electrical and optical confinements and gain inherent in

active region are not enough to allow lasing in a MQW structure. This has been verified experimentally.

Strained-layer superlattice (SLS) lasers which benefit from better optical confinement and more emission wavelength flexibility than offered by a DH structure and a larger gain region than lasers based on a MQW active region are good candidates for high power and high temperature emission between 3.8 and 5 μm. High temperature operation is enhanced with SLS lasers by the suppression of Auger recombination mechanisms with the large number of interfaces and compressive strain inherent with these lasers.[iii]

As an example, Figure 4 shows the calculated layer thickness (in our design the well thickness is equal to the barrier thickness) dependence of emission wavelength for an $InAs_{0.95}P_{0.05}/InAs_{0.75}Sb_{0.25}$ SLS structure that has 0.8 % mismatch from InAs. The Kronig-Penney model, including the strain induced band edge shifting, has been used for the calculation. The flat dotted line represents the emission wavelength of an InAsSb alloy with 0.8 % mismatch from InAs which can only have an emission wavelength at $\lambda = 3.7$ μm. Alternatively, by changing the layer thickness in the superlattice, the emission wavelength can be tuned from 3.3 to 4.5 μm independent of its lattice constant. Therefore, the SLS structure allows the structure to have longer emission wavelength (> 4 μm) with a non-prohibitive mismatch from InAs substrate.

Additionally, the SLS active region allows for more gain than MQW structures. Although the gain per unit length for the MQW is larger, the actual active region thickness is much larger for the superlattice laser.

As a result of its complexity and importance to laser performance, the SLS active region needs to be studied both experimentally and analytically. There are three superlattice material alloys that have the ability to emit between 3.8-5 μm: $InAs_{1-x}Sb_x/InAs_{1-y}P_y$, $InAs/InA_{1-x}sSb_x$, and $InAs_{1-x}Sb_x/InAs_{1-y}Sb_y$. The $InAs_{1-x}Sb_x/InAs_{1-y}Sb_y$ material system is considered as a single system even though both $InAs_{1-x}Sb_x/InAs_{1-y}Sb_y$ and $InAs/InA_{1-x}sSb_x$ active regions can be made from it. The advantages and disadvantages of each system have been qualitatively determined and are shown in

Figure 5.
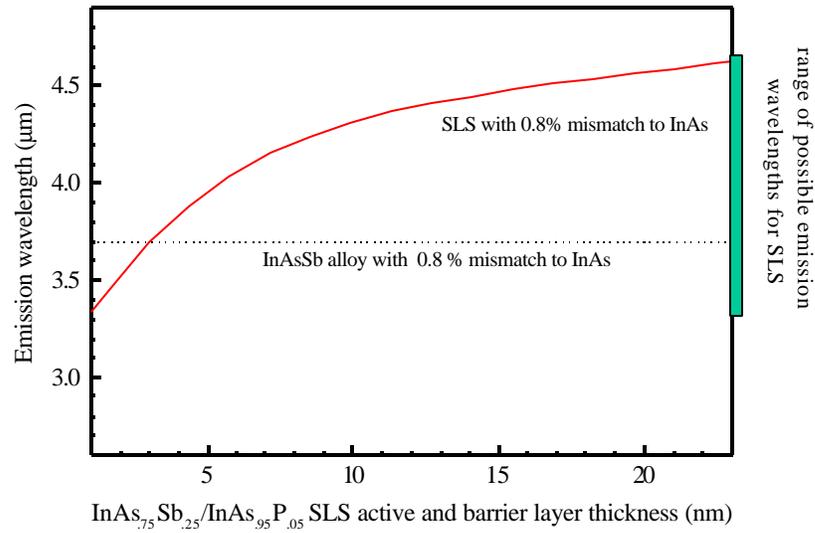
Figure 4. Calculated layer thickness (in our design the well thickness is equal to the barrier thickness) dependence of emission wavelength for an InAs$_{0.95}$P$_{0.05}$/InAs$_{0.75}$Sb$_{0.25}$ SLS structure that has 0.8 % mismatch from InAs.

Possible Materials (barrier/well)	Advantages	Disadvantages
InAs$_{1-x}$Sb$_x$/InAs$_{1-y}$Sb$_y$	• Type-II alignment allows for longer λ	• Reduces radiative recombination efficiency
InAsP/InAsSb	• Flexibility to choose superlattice strain • Wide range of emission	• Low optical confinement • Coupling is less with high P content

Figure 5. Advantages and disadvantages for superlattice material systems with $\lambda \ge 3.8 \ \mu m$.

      The fact that the InAs$_x$Sb$_{1-x}$/InAs$_y$Sb$_{1-y}$ material system is type-II is both an advantage and disadvantage. The type-II nature allows a large range of emission flexibility. However, since the electrons and holes are separated spatially from each other, the overlap integral is smaller leading to a low radiative recombination efficiency. The InAs$_{1-x}$Sb$_x$/InAs$_{1-y}$P$_y$ material system offers the benefits of being able to compensate the strain of the superlattice. This results

4

because InAsP and InAsSb are under tensile and compressive strains respectively to InAs substrate. The two disadvantages associated with this alloy are a consequence of using a phosphorous-based alloy. First, the phosphorous decreases the refractive index, which decreases the confinement factor. Second, the large conduction band offset decreases the uniformity of electron injection.

2. Growth, Characterization, and Measurement of Strained-Layer Superlattice Lasers

All of the strained-layer superlattice active region structures were grown on (100) oriented Te-doped InAs substrates in an EMCORE vertical metal-organic chemical vapor deposition (MOCVD) reactor using trimethylindium (TMIn), trimethylantimony (TMSb), arsine (AsH_3), and phosphine (PH_3) as the sources and tertaethyltin (TESn) and Diethylzinc (DEZn) as the n-type and p-type dopants respectively.

Several growth parameters that have important effects on the final emitter have been optimized. The main parameters are growth temperature, growth rate, III/V ratio, and switching sequence. The effects of these parameters on the quality of the sample have been closely studied by structural, optical, and electrical characterization techniques. The crystal structure is investigated with high resolution x-ray diffraction, scanning electron microscopy, and atomic force microscopy. The optical properties are revealed with photoluminescence measurements. Finally, electrochemical capacitance-voltage measurements are performed on the epilayers to provide accurate electrical characterization.

The growth and characterization of the InAsSb/InAsP and InAsSb/InAsSb strained layer superlattice will be described in details in the sections below together with the fabrication and measurement of the laser devices.

2.1 InAsSb/InAsP/InAs Strained Layer Superlattice Lasers

In the design of these lasers that emit at a specific wavelength, either the thickness of the superlattice determines the composition or visa versa. Initially, we chose that the thicknesses of the superlattice layers equal. Additionally, since the large band offset of InAsP on InAsSb decreases the carrier uniformity and coupling between wells, its thickness should be kept small. Using these design considerations, it has been determined that using the $InAs_{1-x}Sb_x/InAs_{1-y}P_y$

alloy system with $x \approx 0.75$ and $y \approx 0.05$. The superlattice active region has been intentionally not strain compensated as proposed by Kurtz *et al*[iv] in optically pumped structures. Since those structures were pumped optically, carrier transfer and injection uniformity, inhibited by a strain compensated structure, is not an important design consideration. Instead, thin $InAs_{0.95}P_{0.05}$ layers have been used as the barrier layers to allow for a more uniform electrical carrier distribution.

Using these material compositions, and a 0.8 µm active region to achieve the minimum in threshold current density, the optical and electrical properties of the structure were calculated. The emission wavelength for a given composition has been calculated from the band offsets and is shown in Figure 4. The optical mode and confinement factor were calculated and are shown in Figure 6. The superlattice was considered as a material with properties linearly interpolated from InAsSb and InAsP. As expected, the longer emission wavelength leaks farther into the cladding layers and therefore reduces the confinement factor. This should manifest itself in an increased threshold current density. A confinement factor of ~ 46 % was calculated.
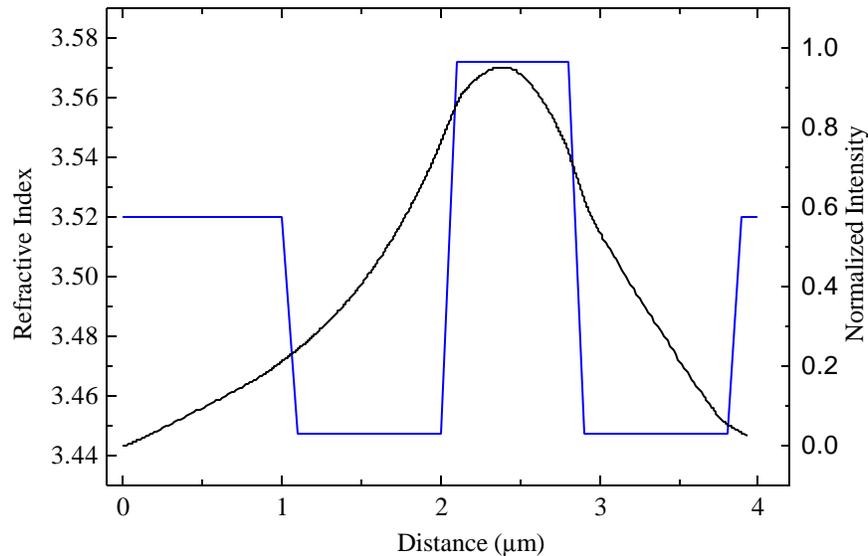
Figure 6. Optical mode and index of refraction profile for the InAsSb/InAsP/InAsSbP strained-layer superlattice laser.

The two materials used in the superlattice were optimized independently. From previous experiments with both DH and MQW InAsSbP based lasers in the Center, the optimum

thermocouple growth temperature is approximately 585 °C.   However, it has also been determined that for $x > 0.10$ in $InAs_{1-x}Sb_x$ the antimony incorporation percentage saturates and increases only slightly with large changes in material flow rates. This has been corroborated by other researchers and is shown below in Figure.
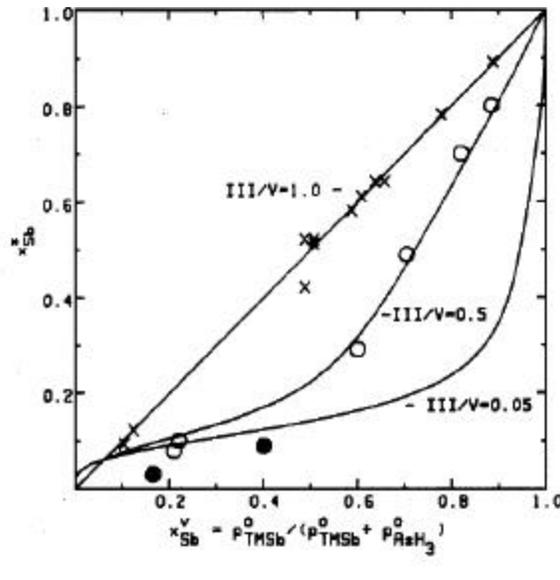
Figure 7. Antimony incorporation into InAsSb versus molar flow rate percentage for various III/V ratios.[v]

Figure shows that with V/III ratios greater than 2, at a constant growth temperature, the greater thermodynamic stability of InAs relative to InSb results in a significant decrease in the distribution coefficient for Sb. Additional experiments have been performed to determine that a V/III ratio greater than 25 is required for high quality growth. Therefore, we were forced to reevaluate the growth temperature for $InAs_xSb_{1-x}$ based superlattices.

Experiments were performed to determine the optimum growth temperature for $InAs_{1-x}Sb_x$ materials with $x > 0.10$. The relationship of Sb incorporation versus growth temperature is illustrated in Figure 8. For constant TmSb and AsH_3 flow rates, the distribution coefficient for TmSb is inversely proportional to temperature.

For an optimum $InAs_{1-x}Sb_x$ with $x > 0.10$, a thermocouple growth temperature of 560 °C was determined. Although lower temperatures produced similar x-ray and PL characterization measurements, carbon incorporation into the epilayer has been reported to increase as growth

temperature is reduced.[vi] Carbon acts electrically as a donor in In-based materials. We have verified that at this temperature the antimony composition varies linearly with source flow rate within the range of material compositions used in this study $(0.0 < x < 0.3)$. This ensures good control of the material composition. With InAsSb, a range of growth rates between 500 to 1500 nm/hr were experimentally examined. Although the x-ray FWHM did not depend strongly on the growth rates, an intermediate growth rate of 1000 nm/hr was used.
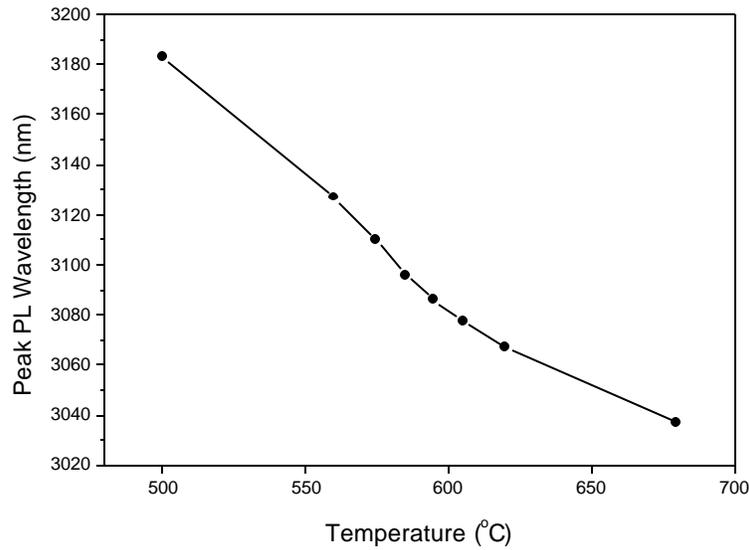
Figure 8. Peak emission wavelength of InAsSb versus growth temperature for constant TmSb and AsH$_3$ flow rates.
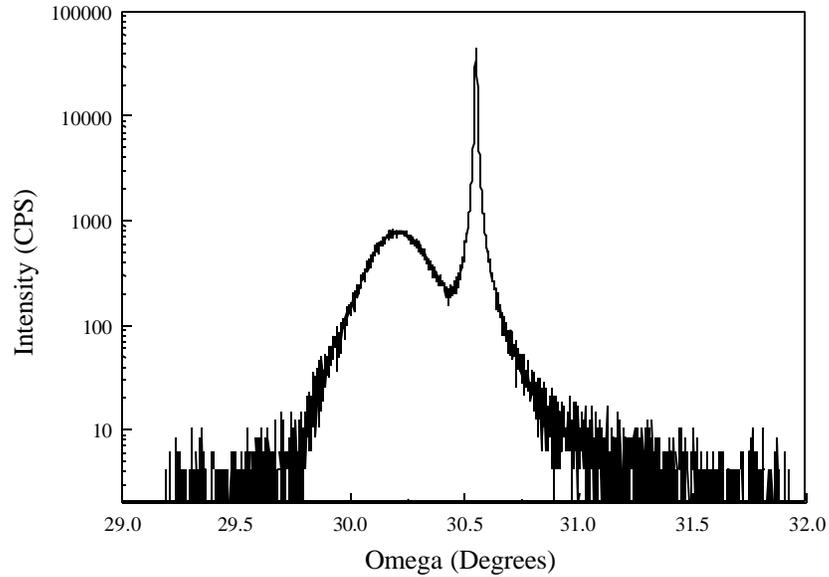
Figure 9. X-ray diffraction spectra for InAsSb mismatched 1 % from InAs.

The x-ray characterization of the $InAs_{0.75}Sb_{0.25}$ layer grown at 560°C showed a relatively narrow FWHM considering the mismatch is just over 1 % and the thickness is only 500 nm. A typical diffraction spectra is shown below in Figure 9. The thickness is 500 nm and was measured by SEM.

Since the epilayer thickness is far greater than the critical thickness (refer to Figure 2), misfit dislocations can been seen under a high power optical microscope. However, with the naked eye the surface is smooth, presumably due to the ability of antimony to act as a surfactant. These dislocations have also been imaged via AFM. Shown in Figure 10 is an AFM image of an individual $InAs_{0.75}Sb_{0.25}$ layer.

9
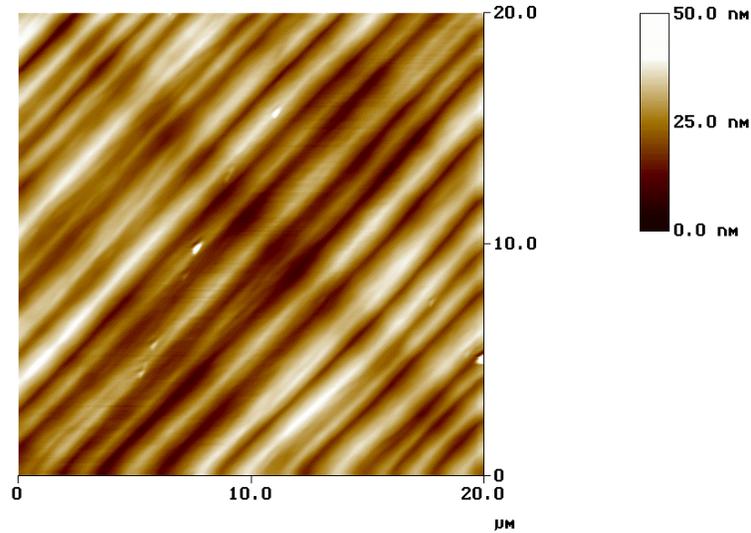
Figure 10. AFM image of an individual 500 nm thick InAs$_{0.75}$Sb$_{0.25}$ layer.

Next, the InAsP alloy was optimized. Despite the relatively large enthalpy of mixing, high quality material was obtained at a growth temperature of 560 °C. Much higher phosphine flow rates were required as a result of the low pyrolysis percentage at the low growth temperature. For the same material composition at 585 and 560 °C the phosphine flow rate was increased from 30 to 80 sccm.

The x-ray characterization of the InAsP epilayer is excellent. It is shown below and its high quality is corroborated by the Pendellosung fringes seen in Figure 11.   The surface is mirrorlike and the AFM characterization demonstrated a roughness of 6 Å for a 20 μm $\times$ 20 μm scan.

10
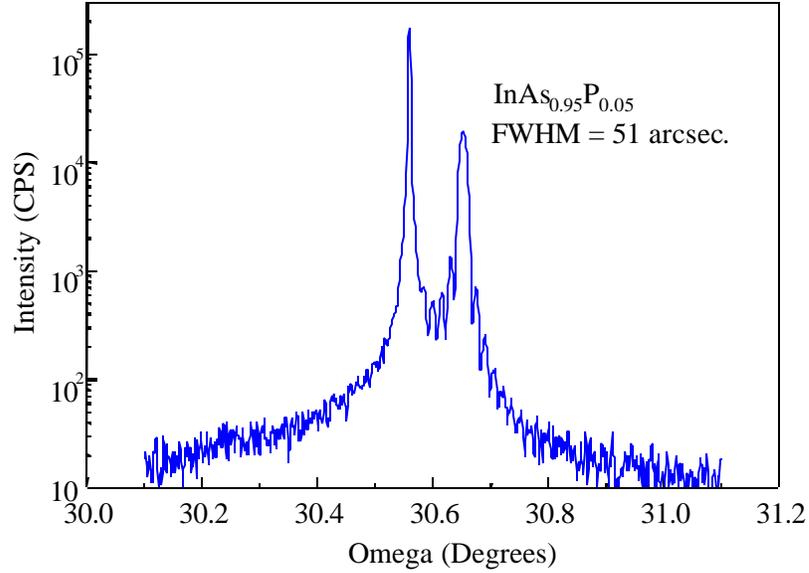
Figure 11. X-ray diffraction spectra of 500 nm thick InAsP.

For the entire active region, the individual materials were simply combined. From our calculations, we used the same thickness for each material of the superlattice. The total period thickness was 100 Å and 80 periods were used in order to have the active region approximately 1 μm. 100 Å thick regions were chosen to allow good tunneling throughout the superlattice. Also, since the switching routine between layers had not been optimized yet, no growth interruption between the layers was used. The entire superlattice region has been grown under the conditions described above. For the entire laser structure, 1.1 μm InAsSbP cladding layers were grown before and after the superlattice growth. These layers were grown with the same doping profile as those used for the previous double heterostructure lasers at the optimized temperature of 585 °C. Since the composition of both ternary and quaternary materials change with temperature, InAs was grown when the temperature was ramped between the cladding and superlattice. At the conclusion of the n-type InAsSbP cladding and InAsP/InAsSb superlattice region, InAs was grown while the temperature was ramped linearly between 585 and 560 °C. The temperature was stabilized for two minutes after the ramping period. A growth rate of 100 Å/min was used to minimize the total thickness of InAs. The structure was completed with a 100 nm p^+ InAs cap layer and is shown schematically in Figure 12.

11

80 period
$InAs_{0.75}Sb_{0.25}/InAs_{0.95}P_{0.05}$

AuGe/Ni/Au

−

+

Ti/Pt/Au

p^+InAs

n $InAs_{0.2}Sb_{0.28}P_{0.52}$

p $InAs_{0.2}Sb_{0.28}P_{0.52}$
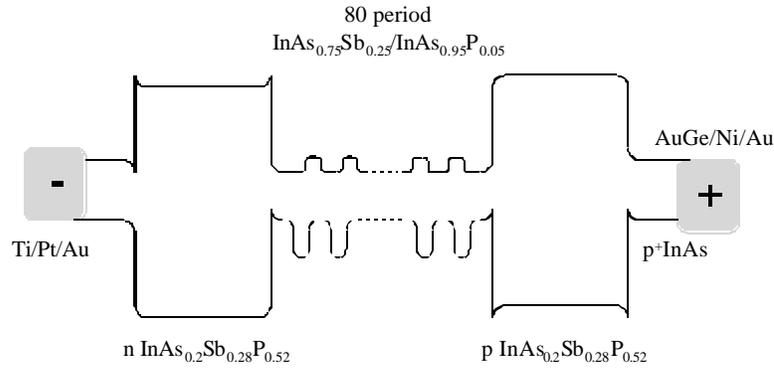
Figure 12. Schematic band alignments of a InAsSb/InAsP strained-layer superlattice injection laser.

The morphology of the laser structure was. The x-ray diffraction spectra has been measured and compared with theoretical calculations of the spectra. They are shown in Figure 13. The high crystalline quality of the strained superlattice structure is confirmed via x-ray measurements and by the three orders of satellite peaks observed in the spectra. These measurements were used to determine the average strain of the superlattice to be 0.79 %. This has been compared to the theoretically predicted mismatch of 0.78%. The peaks are well aligned and are periodic which demonstrates that the period is the designed thickness and was consistent throughout the growth. The measured period from the superlattice satellite peaks is 98 Å while the design period was 100 Å. However, the FWHM is far greater for the measured spectra. This is most likely due to an interfacial layer in between the two layers. This can be minimized via the optimization of the switching routine.
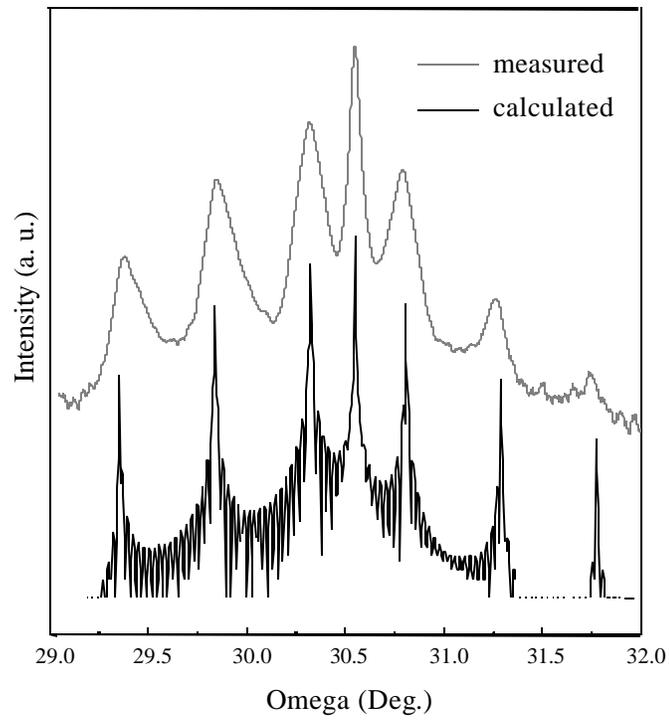
Figure 13. Measured and calculated x-ray diffraction spectra for an InAsSb/InAsP superlattice laser.
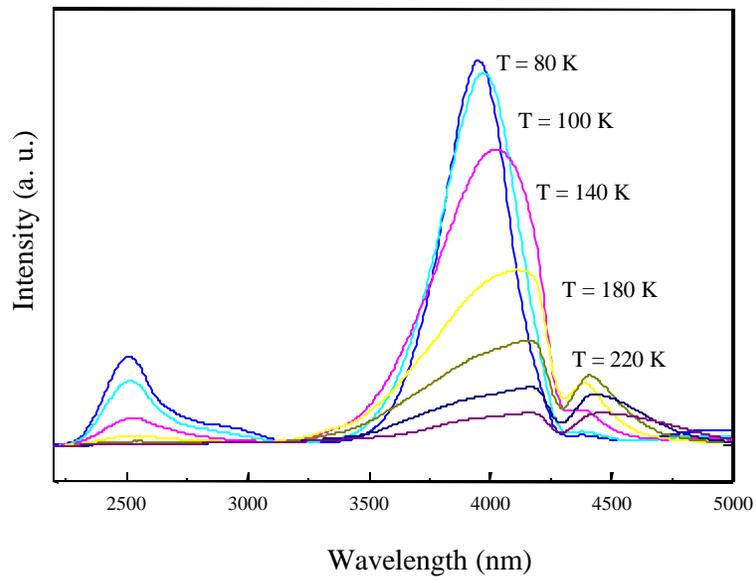
Figure 14. PL spectra for an InAsSb/InAsP superlattice laser.

The photoluminescence versus temperature is also provided below in Figure 14. The peak emission wavelength is 3.95 μm with a narrow FWHM of only 29 meV at 77 K. From our previous experience, these properties are promising for laser emission.

Broad–area laser diodes with a stripe width of 100 μm were fabricated using a lift-off process, in which the p^+ InAs contact cap layer was etched away between the stripes. After ohmic contacts were deposited, individual diodes were cleaved and mounted p-side up on copper heat sinks by indium bonding. Uncoated laser diodes of cavity lengths varying between 400 and 1800 μm were prepared, mounted in a cryostat and then measured.

Figure 15 shows the PI curve and emitting spectra for the laser under pulsed operation at T = 100 K. The output power was measured to be 546 mW with a corresponding threshold current density of 100 A/cm^2 and a differential efficiency 30 % for the cavity length of 1800 μm. From the emitting spectra in the inset of Figure 15, several longitudinal modes, centered around 4.08 μm, can be observed. Continuous wave measurements, shown in Figure 16, resulted in an output power of 94 mW per two facets with a differential efficiency of over 30 %. As mentioned previously, at higher currents, Joule heating becomes significant and is most likely the predominant limiting mechanism at these high powers.[1] Additionally, from the emitting spectra dependence on injection current and temperature, the actual temperature of the junction is estimated to be 20 K greater than that of the heat sink. The highest operating temperature for this laser was 125 K and the threshold current density dependence upon temperature gave a $T_o = 27$ K. The perpendicular far-field divergence was confirmed by several measurements to be 28°.

---

[1] A. Rybaltowski, Y. Xiao, D. Wu, B. Lane, H. Yi, H. Feng, J. Diaz and M. Razeghi, *Appl. Phys. Lett.* **71** 2430 (1997).
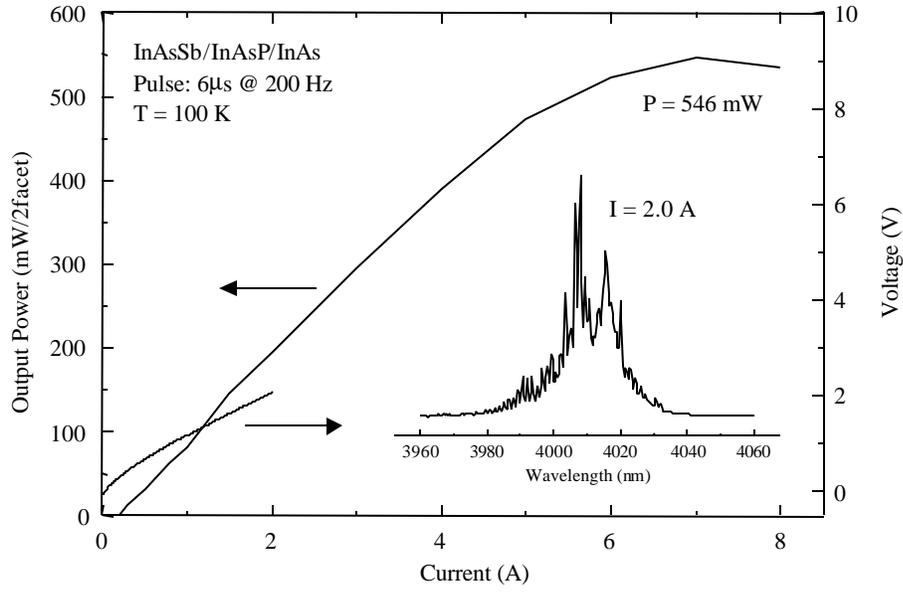
Figure 15. Light output vs. pulsed current of a InAsSb/InAsP strained-layer superlattice laser at T = 100 K. The inset shows the emission wavelength at 80 K.
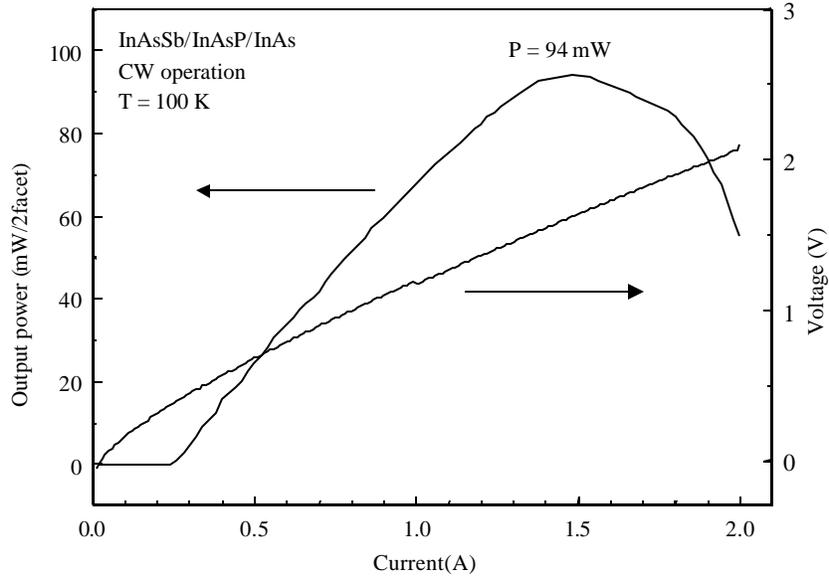

Figure 16. Light output vs. current and current versus voltage curve for cw operation of a InAsSb/InAsP strained-layer superlattice laser at T = 100 K.

2.2 InAsSb/InAs(Sb)/InAs Strained Layer Superlattice Lasers

The InAsSb/InAs, $InAs_{1-x}Sb_x/InAs_ySb_{1-y}$ superlattice active regions do not suffer from the problems resulting from the InAsP and have the advantages of large emission tunability because of the type-II band alignment of InAsSb and InAs. However, there are disadvantages for these two superlattice systems. First, associated with the type-II alignment, there is a reduced wave function overlap resulting in a lower optical matrix element and finally a reduced radiative transition probability. Additionally, since InAsSb is compressively strained to InAs, the superlattices will also be strained.

As a result of the strained superlattice to be used in the active regions, there will be misfit dislocations within the active region. In an effort to reduce the number of dislocations and therefore the carriers lost to these dislocations, the thicknesses used should be minimized. The optical properties of the structures have been calculated. The optical wave is not symmetric with the waveguide as a result of the air interface ($n_{air} = 1$) at the end of the structure. The most important parameter, the optical confinement factor, was calculated to be ~ 50 % for $\lambda = 4.0$ μm. This compares favorably with the InAsSb/InAsP structure emitting at the same wavelength considered in the previous section.

In the section 0, the growth of $InAs_{1-x}Sb_x$ with values of x~25% was described in detail. High values of x were required because of the large conduction band offset that InAsP creates in the material. Since InAs and InAsSb are used as the barrier materials in InAsSb/InAsSb and InAs/InAsSb superlattice regions, much smaller values of x are required. This will allow for higher growth temperatures that reside closer to the optimum growth temperature. Calculations show that for superlattices with the same thickness for well and barrier, x is no greater than 15 %. Furthermore, for both of the active region superlattices, 100 Å thick layers will be grown. This ensures that they are below the critical thickness and that the number of misfit dislocations is kept to a minimum.

Despite the fact that the growth temperature is closer to the InAsSb optimum growth temperature, the switching routine is more critical for these superlattices than for the InAsSb/InAsP superlattices. Since antimony has a long residence time during the growth process, a balance must be made between the growth interruption and change in antimony flow rates. Too long an interval translates into complete antimony removal, which results in an arsenic rich InAsSb interface. Too short a growth interruption will result in non-abrupt

16

interfaces. The growths of the barriers for both of the superlattices focused upon are routine. The barriers are either InAs or InAsSb with an antimony composition similar to that used for the active region for double heterostructure lasers.

As mentioned previously, there were several growth related issues with the superlattice active region. They are not so much the single layers, but how those layers are combined into the superlattice. However, as before, the single layers were grown, characterized, and optimized and then the superlattice was simply a compilation of the single layers.

First, the active well materials were grown. The compositions were determined from x-ray diffraction and were grown for percentages as high as 14 %. Although, at this percentage, these epilayers were at or slightly below the theoretical critical thickness, these samples of 400 nm in thickness were mirrorlike. The x-ray for a sample corresponding to an antimony incorporation percentage of 9 % is shown below in Figure 17.
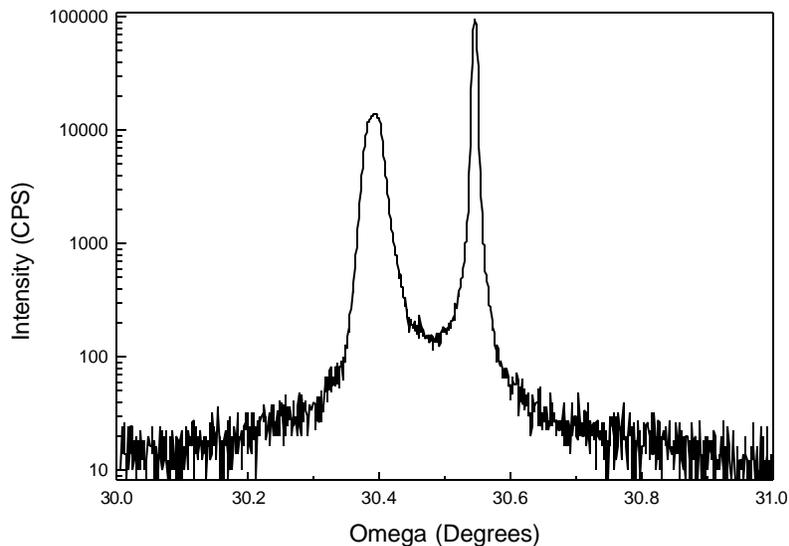
Figure 17. X-ray diffraction pattern of an 400 nm thick InAsSb layer with 9% antimony.

AFM scans did not show any misfit dislocations. This is presumably due to the surfactant nature of antimony. However, AFM did show that the atomic steps were two or three monolayers high with large antimony percentages instead of one monolayer steps for small antimony percentages. The growth rate was determined via SEM and was targeted to be

17

approximately 160 Å/min. This growth rate was used to calculate the growth time for the layers in the superlattice.

Finally, the InAs and InAsSb barrier layers were grown. For InAs homoepitaxy, the characterization is excellent. The x-ray FWHM is limited by the resolution of the diffractometer and the AFM confirms atomically flat layers. The same is true for the $InAs_{0.95}Sb_{0.05}$ epilayers. The AFM characterization for a 400 nm sample is also very good; the atomic steps resulting from the miscut of the substrate are seen. The x-ray FWHM is ~ 45 arcsec and the roughness of 10×10 μm scan is 4 Å.

Since the photoluminescence of the InAsSb layers results from an energy gap below that of the InAs substrate, the PL from single layers is not a good indication of the material quality/uniformity (carriers transfer to substrate or recombine at surface because of large diffusion length). Instead, PL results of the superlattice were evaluated and are shown below in Figure 18.

The superlattice active regions for both InAsSb/InAs and InAsSb/InAs consisted of 100 periods. X-ray diffraction confirmed the thicknesses of the well and barrier to be 100 Å each. The morphology of the samples was mirrorlike. However, as a result of the mismatched superlattice, misfit dislocations were formed. These dislocations could be seen via AFM and a typical scan is shown below in Figure 18. Note the very small vertical scale despite the large scan area.
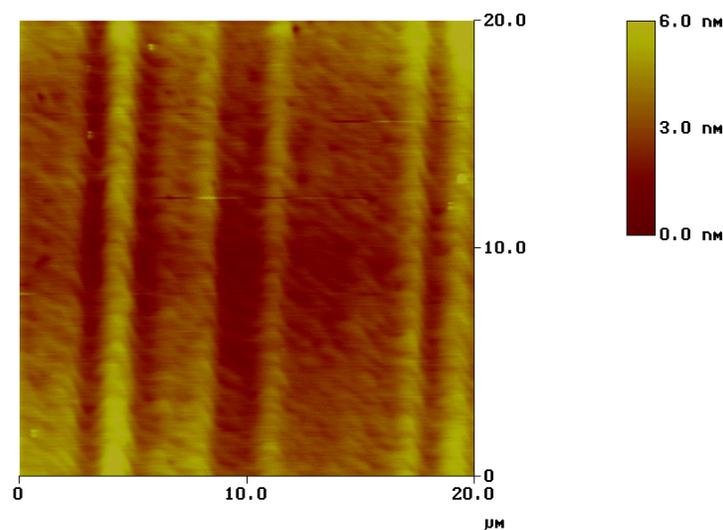

Figure 18. AFM of an InAsSb/InAsSb superlattice.

18

Several switching routines between the superlattice layers were tried. Shown below in Figure 199 are two example x-ray diffraction spectra with different switching routines for an InAsSb/InAsSb superlattice. The top pattern corresponded to no growth interruption while the bottom spectra corresponds to three second interruption between the well and the barrier.
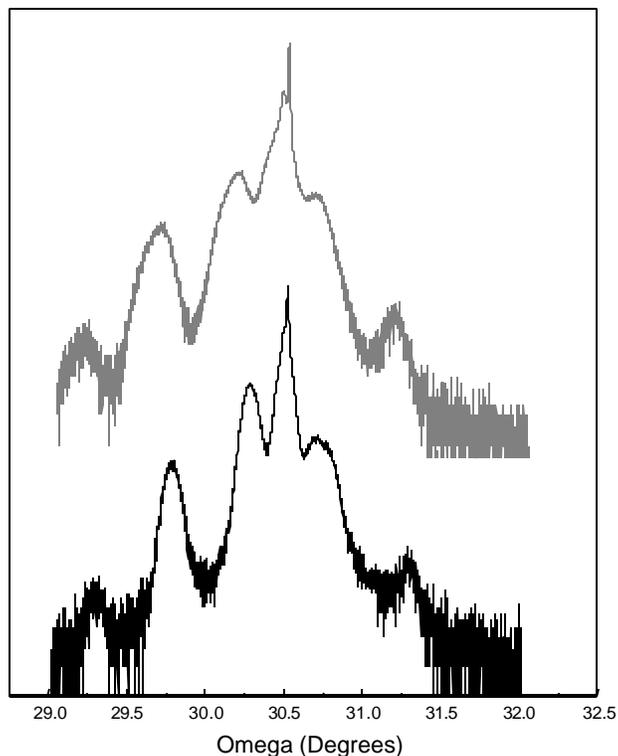

Figure 19. X-ray diffraction spectra for two InAsSb/InAsSb superlattices with different switching routines.

The 0th order satellite peak is mismatched the same on both samples indicating that the superlattice strain is roughly equal. It is clear that the bottom spectra have more abrupt interfaces from the differences in x-ray FWHM. The average strain of the superlattices is 0.59 %.

The photoluminescence versus temperature spectra measurements are provided below in Figure 20. The peak emission wavelength is 3.95 μm with a narrow FWHM of 29 meV. InAsSbP cladding regions were used for confinement. The measurements were performed under relatively low excitation power density in order to reduce Auger recombination which is

proportional to the carrier density $\sim n^3$. The peak emission wavelength at 78 K is $\sim$ 4100 nm and the FWHM is slightly eroded by CO_2 absorption at 4.2 μm. The peaks at 78 and 100 K are roughly the same intensity despite the radiative recombination efficiency being lower at 100 K. This, as mentioned before, is because of the increased diffusion at higher temperatures.
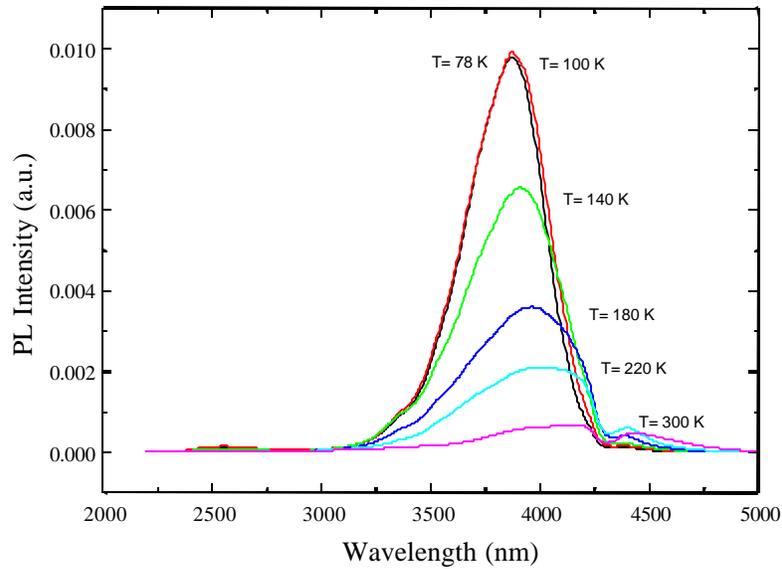

**Figure 20. PL spectra for an InAsSb/InAsSb superlattice.**
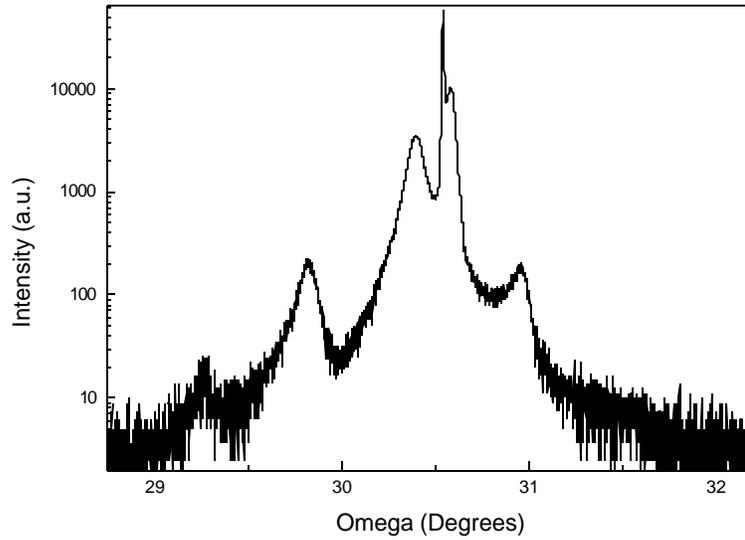
**Figure 21. X-ray diffraction spectra for an InAsSb/InAs superlattice.**
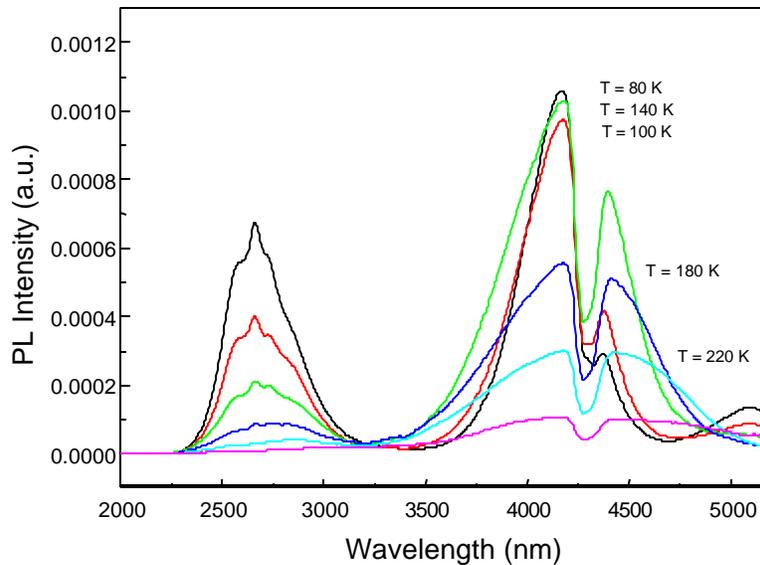
Figure 22. PL spectra for an InAsSb/InAs superlattice. The spectra is distorted at~ 4200 nm as a result of CO_2 absorption.

The x-ray and PL spectra for a typical InAsSb/InAs superlattice is shown below in Figure 21 and Figure 22.

Broad–area laser diodes with a width of 100 μm were fabricated. Optical output power-injection current characteristics were measured in both cw and pulsed mode operation for lasers mounted inside a cryostat with temperatures varying between 77 and 140 K.

For InAs/InAsSb SLS lasers designed to emit at 3.8 µm, *PI* measurements revealed a threshold current density of 67 A/cm^2 and a differential efficiency of 38 %. The pulsed *PI* is shown in Figure 23. The differential efficiency was observed to be constant over the entire range of operating temperatures measured. The highest operating temperature was measured to be 120 K. Under continuous wave operation, these diodes displayed output powers as high as 300 mW at 80 K. The cw PI curve is shown in Figure 24. Furthermore, perpendicular far-field divergence angles and series resistance measurements revealed values of 34 ° (Figure 28) and 0.3 Ω respectively at 78 K. The transparent current density was found to be ~ 47 A/cm^2 from the threshold current density dependence on cavity length. This compares favorably to the values measured for double heterostructure lasers considering the complexity of these lasers. The internal loss was also calculated to be 16 cm^{-1}. These two parameters are shown in Figure 20. Finally, spectral properties of these diodes versus different operating temperatures and injection currents are shown in Figure 21 and Figure 22.
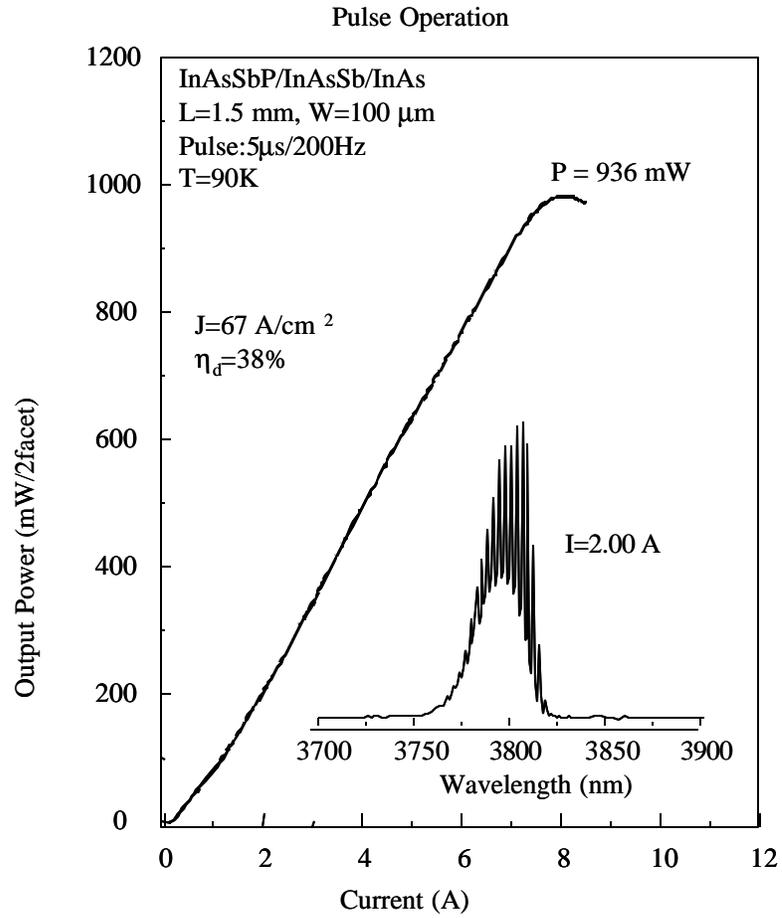
Figure 23. Pulsed output power versus injected current per two facets for an InAs/InAsSb laser at T = 90 K. The emitting spectra, centered around 3.80 mm, is shown in the inset.

CW Operation

InAsSbP/InAsSb/InAs
L=1.5 mm, W=100 μm
CW operation
T=90K

P=300 mW

$J_{th} = 67$ A/cm^2

Output Power (mW/2facet) vs Current (A)
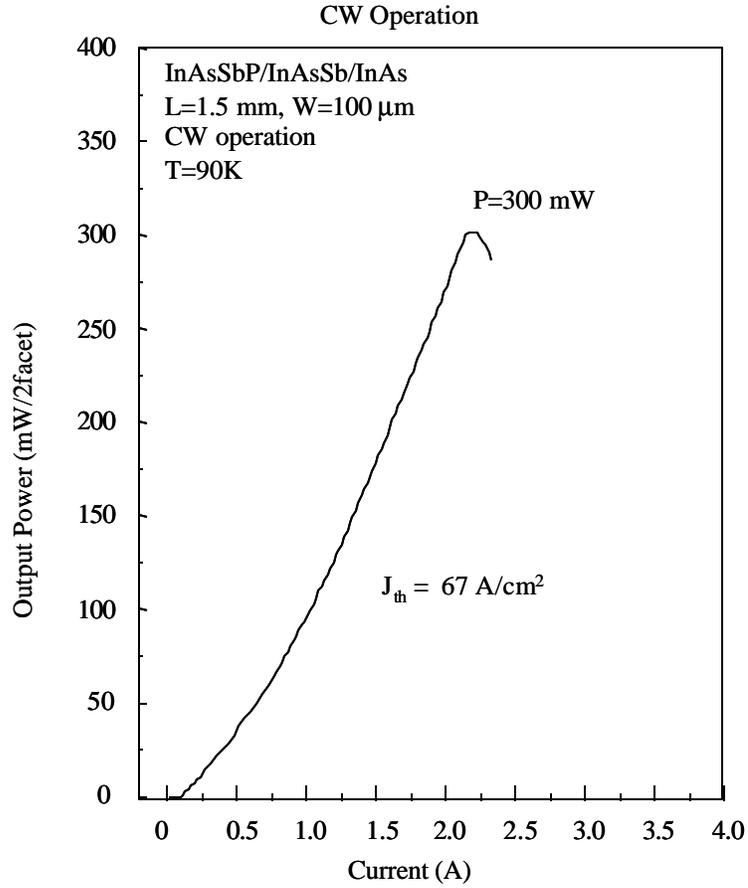
Figure 24. Continuous power for an InAs/InAsSb SLS laser diode with T = 90 K.

InAs/InAsSb
pulse:5 μs/200 Hz
T=79 K, λ=3.8 μm

$J_o \sim 47$ A/cm^2

J_{th} (A/cm^2) vs 1/L (cm^{-1})

InAs/InAsSb
pulse:5 μs/200 Hz
T=79 K, λ=3.8 μm

$\alpha_i \sim 16$ cm^{-1}

1/η_d vs Cavity Length (μm)
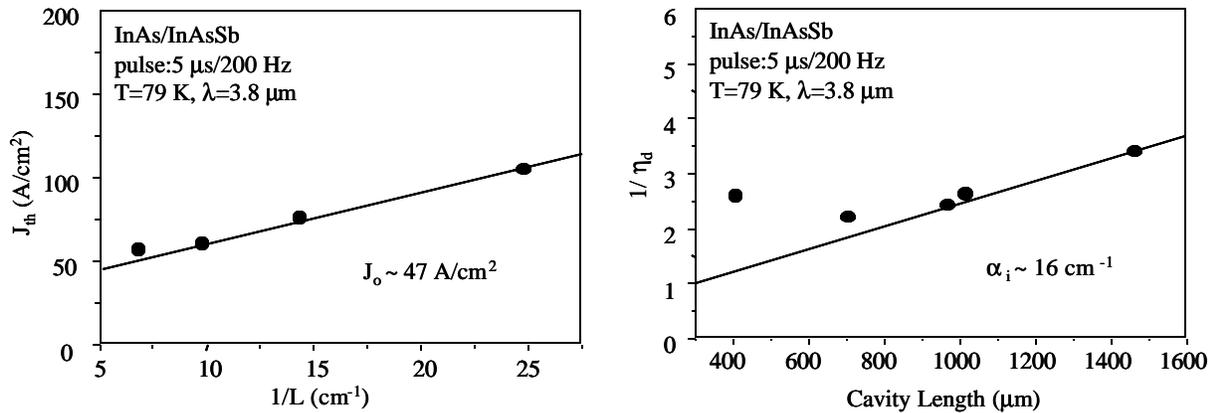
Figure 20. Transparent current density and internal loss measurements for InAsSb/InAs superlattice lasers emitting at 3.80 μm.
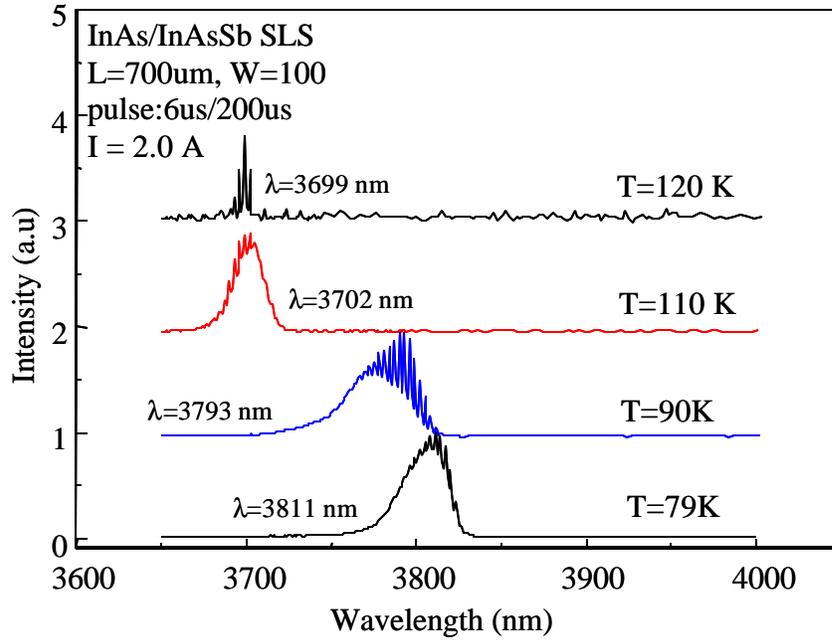
Figure 21. Emitting spectra of an InAs/InAsSb SLS laser for various temperatures.
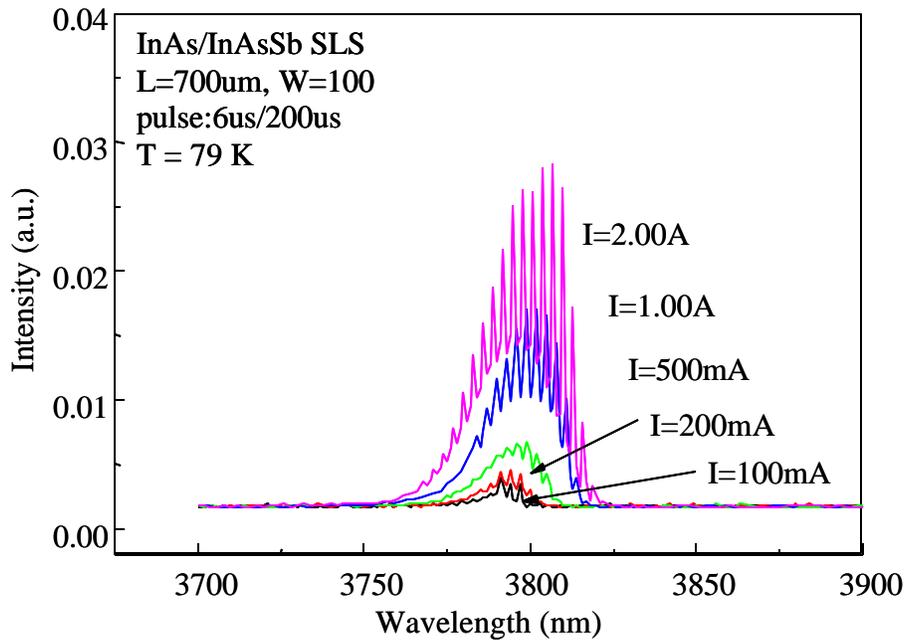

Figure 22. Emitting spectra of an InAs/InAsSb SLS laser for various injection currents.
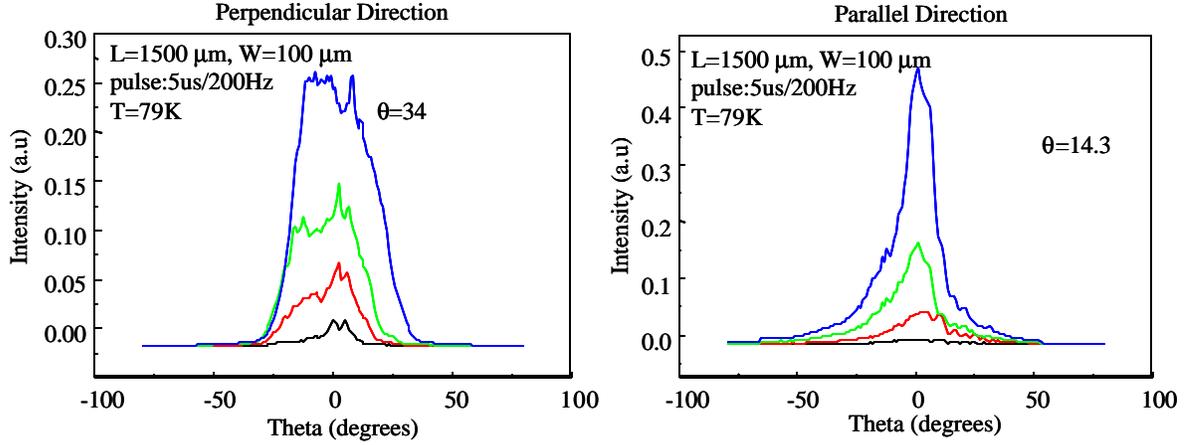
Figure 28. Far-Field divergence angles for both the perpendicular and parallel directions. The different curves are for injection currents beginning with 500 mA and increasing by that amount.

Additional InAs/InAsSb lasers were grown and fabricated to emit with $\lambda = 3.9\text{-}4.0\,\mu m$ and they displayed similar characteristics. In order to increase the emission wavelength, the antimony composition (flow rate) was increased for InAsSb layer within the superlattice active region. Again lasers were fabricated by the methods described above. A typical perpendicular far-field measurement is given in Figure 25. The emitting spectra for several injection currents above threshold are shown in Figure 26. A maximum output power of 842 mW in pulsed mode for a total aperture of $300\,\mu m$ was observed and is shown in Figure 24. Finally the transparent current density and internal loss have been measured and are shown in Figure 27.

Even longer emission has been achieved with InAsSb/InAsSb SLS lasers. Figure 28 shows the *PI* and spectra of an InAsSb/InAsSb SLS laser diode emitting multiple longitudinal modes centered at $4.26\,\mu m$. For lasers with an emission wavelength of $4.26\,\mu m$, we have measured an output power from a single $100\,\mu m$ aperture with $T = 80$ K of 165 mW. *PI* measurements revealed a threshold current density of 300 A/cm^2 and a differential efficiency of 20 %. The differential efficiency was observed to be constant over the entire range of operating temperatures measured. A characteristic temperature of $T_0 = 40$ K was measured from the dependence of threshold current density on temperature. The highest operating temperature was measured to be 140 K. Furthermore, perpendicular far-field divergence angles and series resistance measurements revealed values of $43°$ and $0.3\,\Omega$ respectively at 77 K.
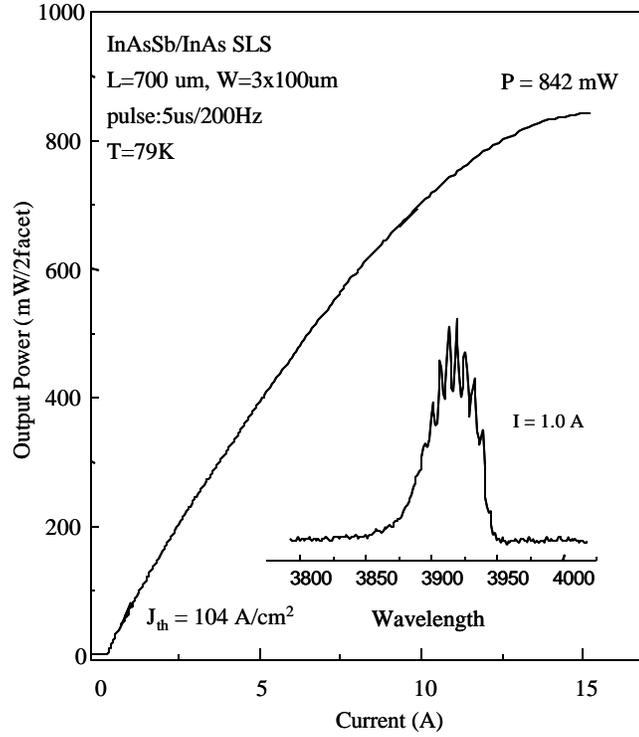
Figure 24. Light output vs. pulsed current curve of a InAsSb/InAs SLS laser at T = 79 K. The inset shows the emission wavelength.
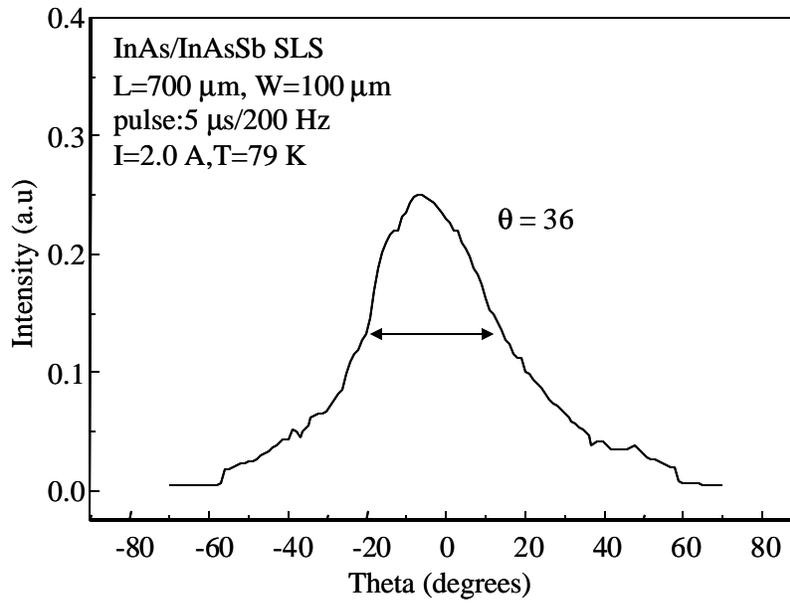

Figure 25. Perpendicular far-field for an InAs/InAsSb SLS with l = 3.9 mm.
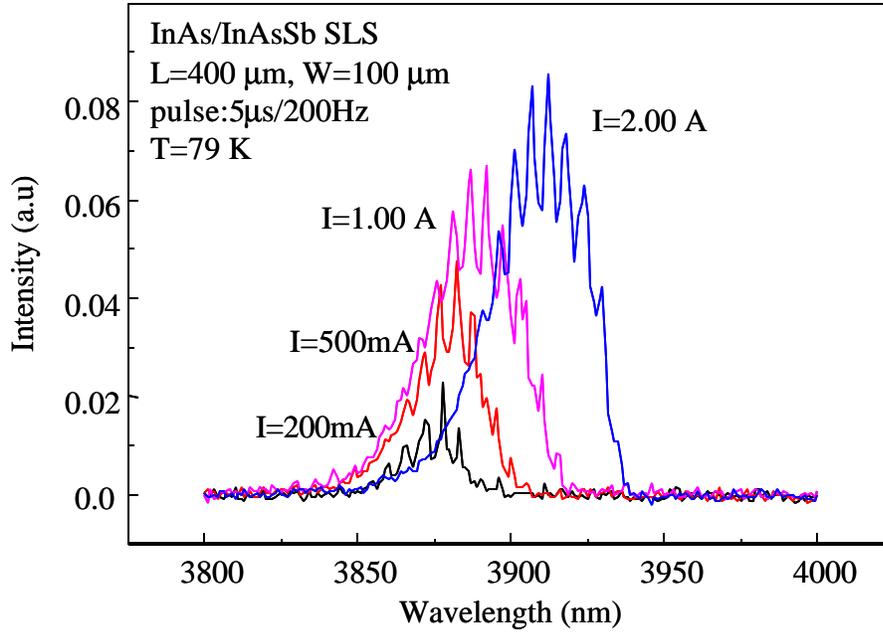
Figure 26. Emitting spectra for an InAs/InAsSb SLS laser for different injection currents.
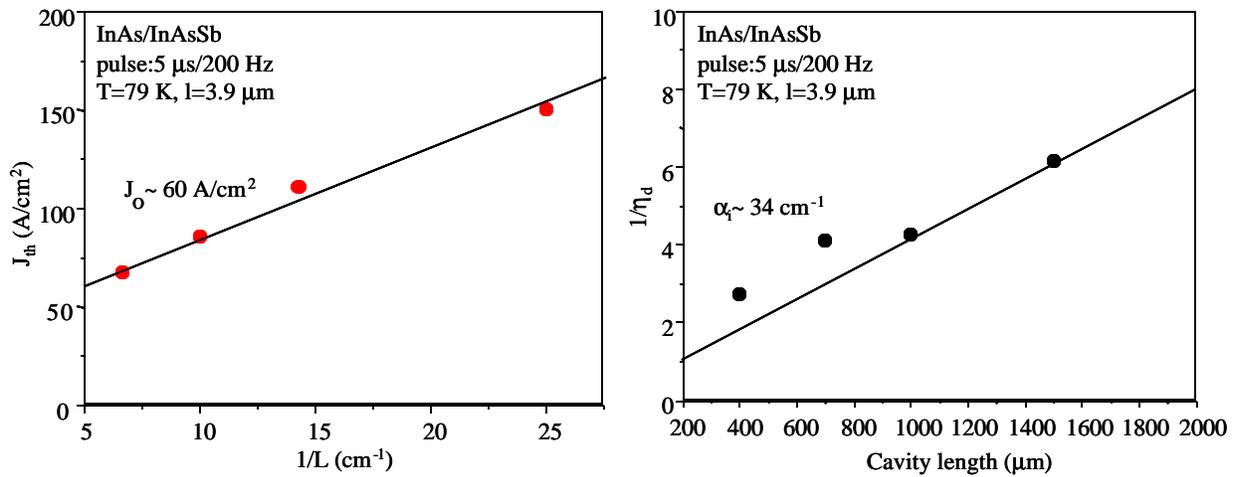

Figure 27. Transparent current density and internal loss measurements for InAsSb/InAs superlattice lasers emitting at 3.9 mm.
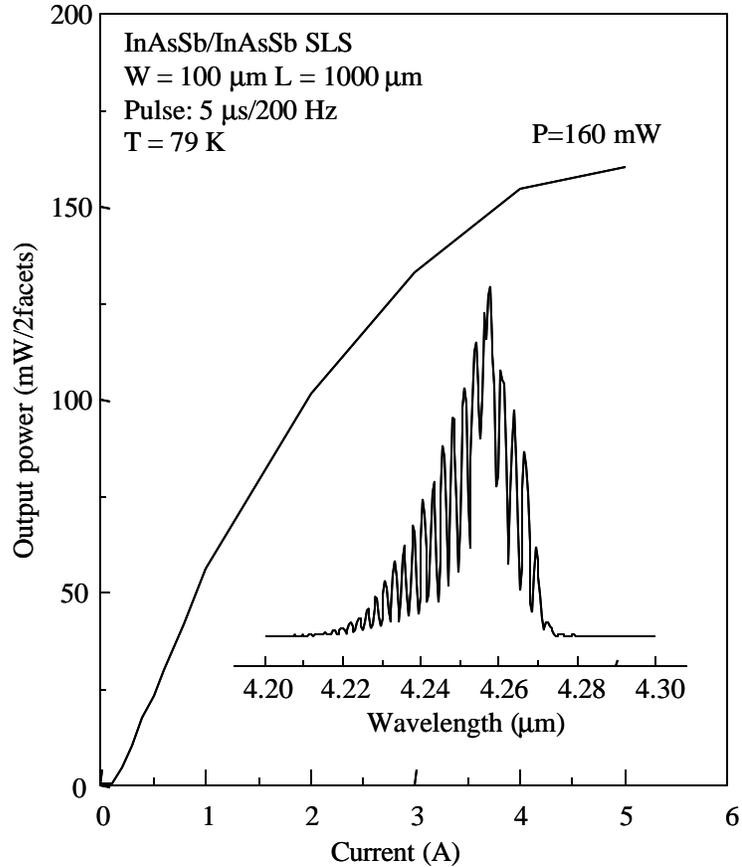
Figure 28. *PI* **curve of a single stripe, 100 period InAsSb/InAsSb laser at T = 80 K. The emission spectrum is shown in the inset.**

Increasing the antimony composition with the superlattice has allowed lasers with an emission wavelength of 4.46 μm to be fabricated. Despite the longer emission wavelengths and therefore the higher Auger and free carrier absorption losses, output powers from a single 100 μm aperture of 199 mW with T = 79 K have been measured This PI curve is shown in Figure 29. The threshold current density was only 160A/cm^2 its dependence upon temperature gave a T_0 of 16 K (Figure 30). The emitting spectra for several injection currents is shown in

Figure 31. Furthermore, these lasers have been fabricated into laser bars and have displayed a maximum output power of 460 mW for a total aperture of 800 μm (Figure 32).
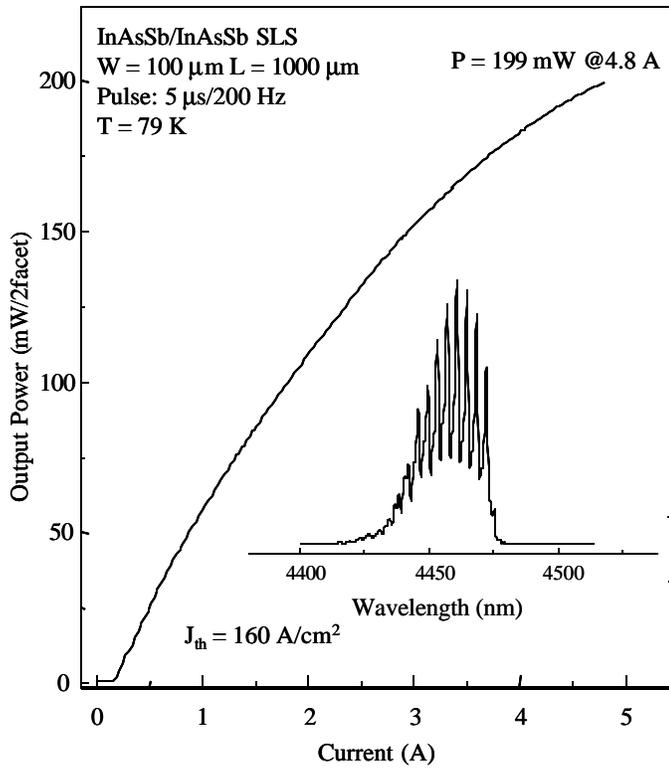
Figure 29. PI curve of a single stripe, 100 period InAsSb/InAsSb laser at T = 80 K. The emission spectrum is shown in the inset.
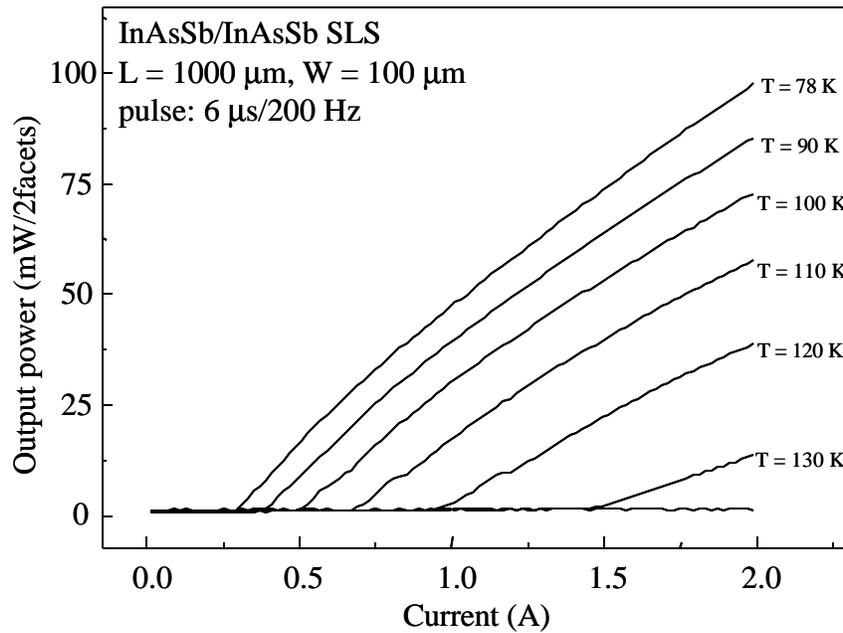

**Figure 30. PI curves for various temperature for an InAsSb/InAsSb SLS with l ~ 4.48 mm**
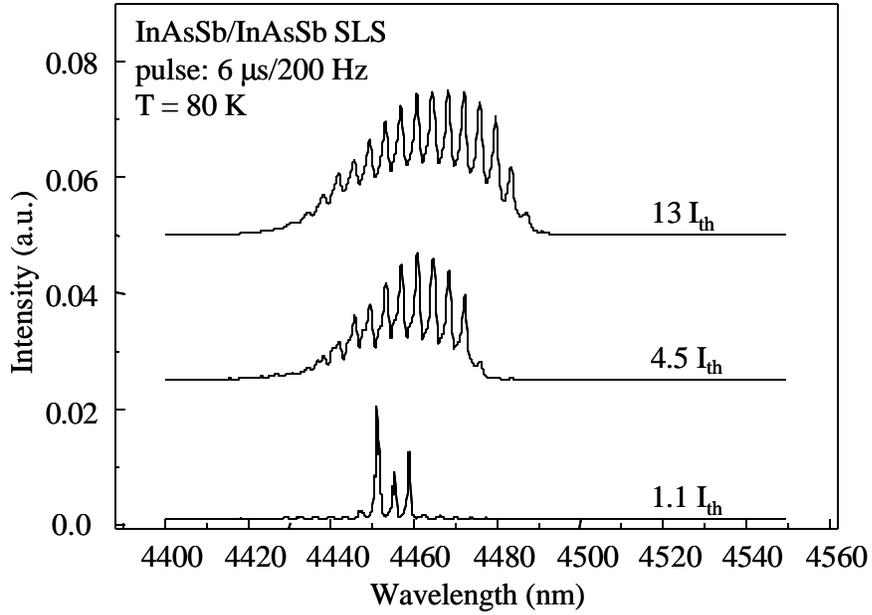
Figure 31. Emitting spectra for an InAsSb/InAsSb SLS laser for several injection currents.
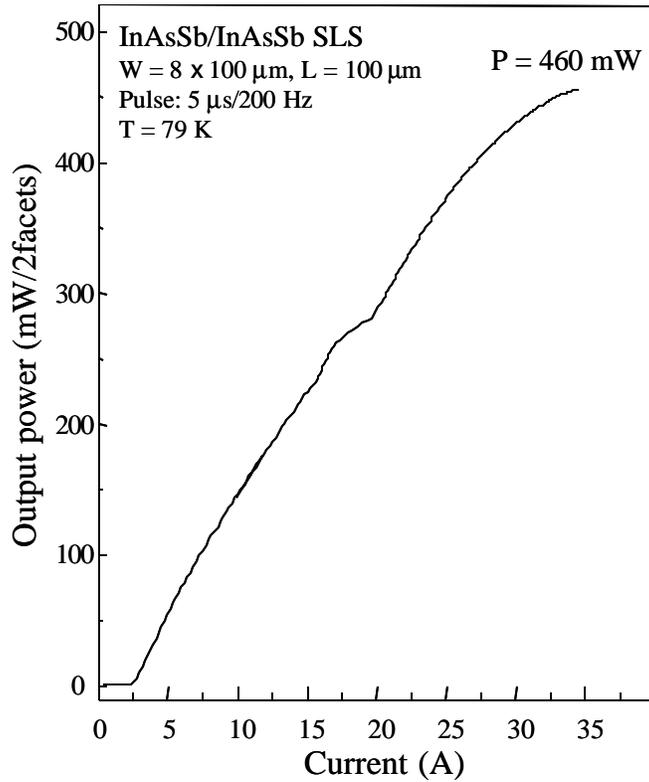
Figure 32. *PI* **curve of an 100 period InAsSb/InAsSb laser at T = 80 K. The total aperture is 800 nm and the emission spectrum is shown in the inset.**

Single stripe InAsSb/InAsSb lasers emitting at $\lambda = 4.76\,\mu m$ have also been measured. A maximum output power of 92 mW under pulsed mode operation for 4.3 A injection current at 79 K is reported (Figure 33). The emitting spectrum reveals multiple longitudinal modes centered at 4.76 μm. *PI* measurements revealed a threshold current density of 393 A/cm^2 and a differential efficiency of over 10 %. The emitting spectra for several injection currents is shown in Figure 35. These lasers have also been fabricated into laser bars and have displayed a maximum output power of 230 mW for a total aperture of 1 mm (Figure 34). This is the longest reported emission wavelength for injection interband lasers with this material system.
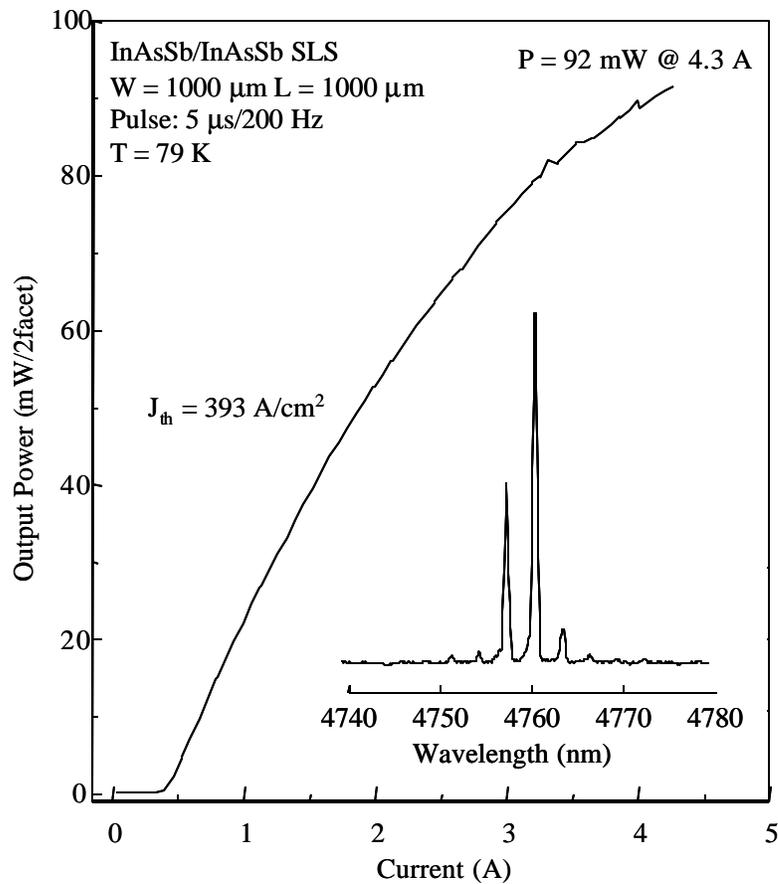

Figure 33. PI curve of a single stripe, 100 period InAsSb/InAsSb laser at T = 79 K. The emission spectrum is shown in the inset.
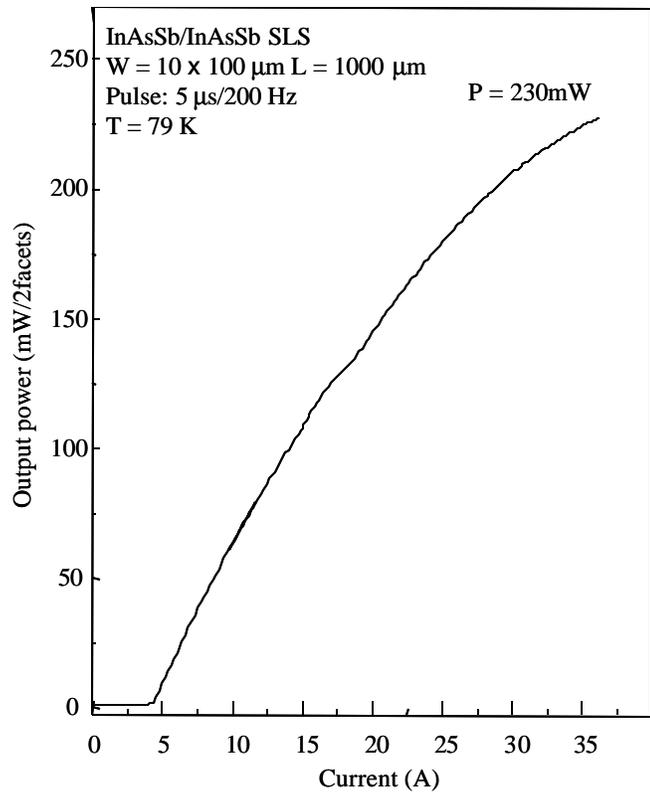
Figure 34. *PI* curve of an 100 period InAsSb/InAsSb laser at T = 80 K. The total aperture is 1000 mm.
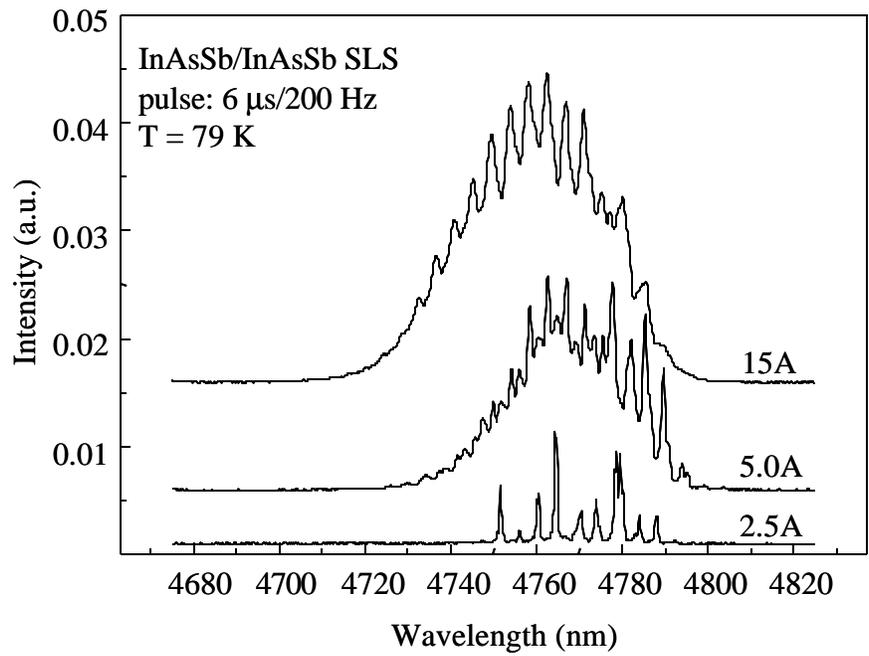

Figure 35. Emitting spectra for an InAsSb/InAsSb SLS laser for several injection currents.

3 Conclusions

InAsSbP based strained-layer superlattice lasers which benefit from better optical confinement and more emission wavelength flexibility than DH or MQW lasers have been designed and fabricated for high power and high temperature emission about $4\,\mu$m. The modeling of the InAsSb/InAsP, InAsSb/InAsSb and InAsSb/InAs strained layer superlattice as the active region has been setup. MOCVD growth of the strained layer superlattice laser was optimized. The quality of the grown samples has been appraised by structural, optical, and electrical characterization techniques. Lasers fabricated with the InAsP/InAsSb superlattice alloy produced laser oscillation at $\lambda = 4.0\,\mu$m with output powers as high as 546 mW and 94 mW in pulsed and cw modes respectively. The InAs/InAsSb superlattice alloy also has been used for the active region of lasers with $\lambda = 3.8\text{-}4.0\,\mu$m. At low temperature, these lasers emit with very high power: up to 1.0 W with $\lambda = 3.8\,\mu$m, and 842 mW with $\lambda = 4.0\,\mu$m. Finally, InAsSb/InAsSb superlattice lasers have also been employed and have demonstrated a wide range of emission flexibility. Laser oscillation between 4.2 and $4.8\,\mu$m have been measured with powers as high as 460 mW.

[i] J. W. Matthews, and A. E. Blakeslee, *J. Cryst. Growth* **27** 118 (1974).

[ii] R. People, and J. C. Bean, *Appl. Phys. Lett*. **47** 322 (1985).

[iii] H. Mohseni, V. Litvinov, and M Razeghi, *Phys. Rev. B*, **58** 378 (1998).

[iv] S. R. Kurtz, A. A. Allerman, and R. M. Biefeld, *Appl. Phys. Lett.*, **70** 3188 (1997).

[v] R. M. Biefeld, *J. Cryst. Growth,* **75** 225 (1986).

[vi] C. H. Chen, C. T. Chiu, G. B. Stringfellow, and R. W. Gedridge, *J. Cryst. Growth* **124** 88 (1992).

DISTRIBUTION LIST

DTIC/OCP
8725 John J. Kingman Rd, Suite 0944
Ft Belvoir, VA 22060-6218   1 cy

AFRL/VSIR
Kirtland AFB, NM 87117-5776   1 cy

AFRL/VSIH
Kirtland AFB, NM 87117-5776   1 cy

Northwestern University
Center for Quantum Devices
2225 N. Campus Drive
MLSB Room 4051
Evanston, IL 60208-3129   1 cy

Official Record Copy
AFRL/DELS/Mr. Ron Kaspi   3 cys